Chapter 2

Experimental Techniques

This chapter presents the experimental techniques used in our studies. To understand the structure-function relations in carbon nanotube (CNT) foams, we fabricated various aligned CNT foams with different microstructures, such as vertically aligned CNT (VACNT) foams with varying bulk densities, helically coiled CNT (HCNT) foams, and micro-architectured VACNT foams. Section 2.1 provides detailed methodologies used for the synthesis of VACNT foams, HCNT foams, and micro-architectured VACNT foams. The Figure 2.1 provides an overview of the various VACNT foams we synthesized. The figure also shows the different geometries and microstructures studied, ranging from nano- to millimeter- scales. Figure 2.1 can be referred to as a summary figure of the materials presented in this dissertation.

We characterized the structure of the CNT foams (e.g. alignment of the CNTs, intrinsic mass density gradients) using synchrotron x-ray scattering and mass attenuation. Section 2.2 presents the experimental and data reduction methodologies used for obtaining the structural characteristics of CNT foams.

We characterized the mechanical response of the CNT foams using quasistatic and dynamic compression experiments. Section 2.3 provides a brief introduction to the instrument and methods used for quasistatic compression testing. Section 2.4 presents a detailed description of the new experimental testing setup we developed for the characterization of complex soft materials at high-rate finite deformations. It includes an introduction and the motivation for developing such an experimental platform, a complete description of the instrumentation, the data reduction methods, and the validation of the technique using VACNT foams as the test samples.
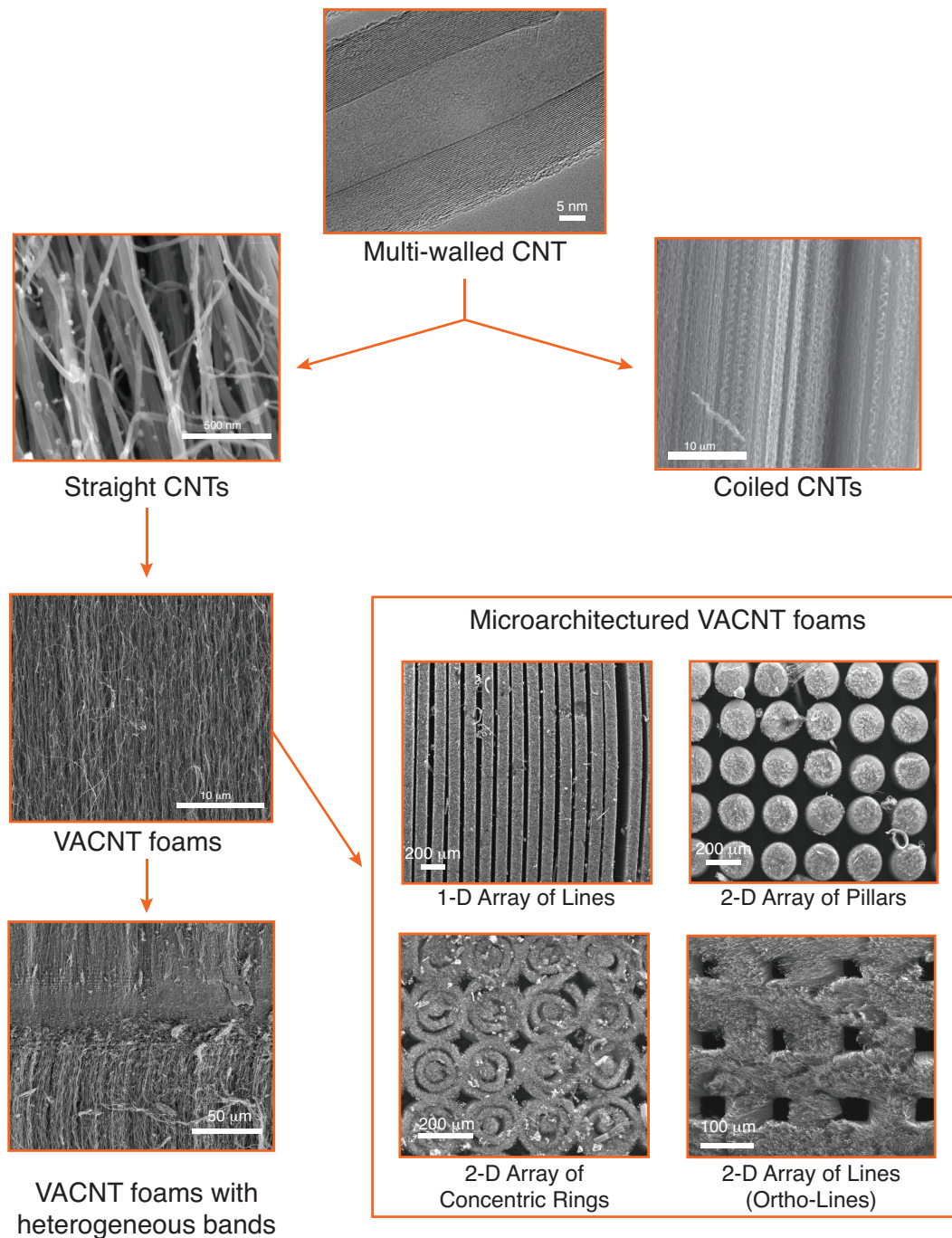
Multi-walled CNT

Straight CNTs

Coiled CNTs

VACNT foams

VACNT foams with
heterogeneous bands

Microarchitectured VACNT foams

1-D Array of Lines

2-D Array of Pillars

2-D Array of
Concentric Rings

2-D Array of Lines
(Ortho-Lines)

Figure 2.1. Overview of the CNT-foams and of the different features analyzed at different scales. All the CNT foams studied are composed of multi-walled CNTs (MWCNTs).

2.1   Synthesis of vertically aligned carbon nanotube foams

As mentioned in the introductory chapter, floating-catalyst and fixed-catalyst thermal chemical vapor deposition (tCVD) processes are commonly used to synthesize long VACNT foams with high yield. We also adopted these two synthesis techniques to grow our aligned CNT foams and the technical details specific to the synthesis of samples presented in this dissertation are provided in this section. Section 2.1 is divided into five subsections where the first four subsections provide methods for the floating-catalyst synthesis of VACNT foams, the fixed-catalyst synthesis of VACNT foams, the floating-catalyst synthesis of HCNT foams and the synthesis of micro-architectured VACNT foams, respectively; and the fifth subsection provides a brief description concerning toxicity and safe sample handling practices used for our experiments.

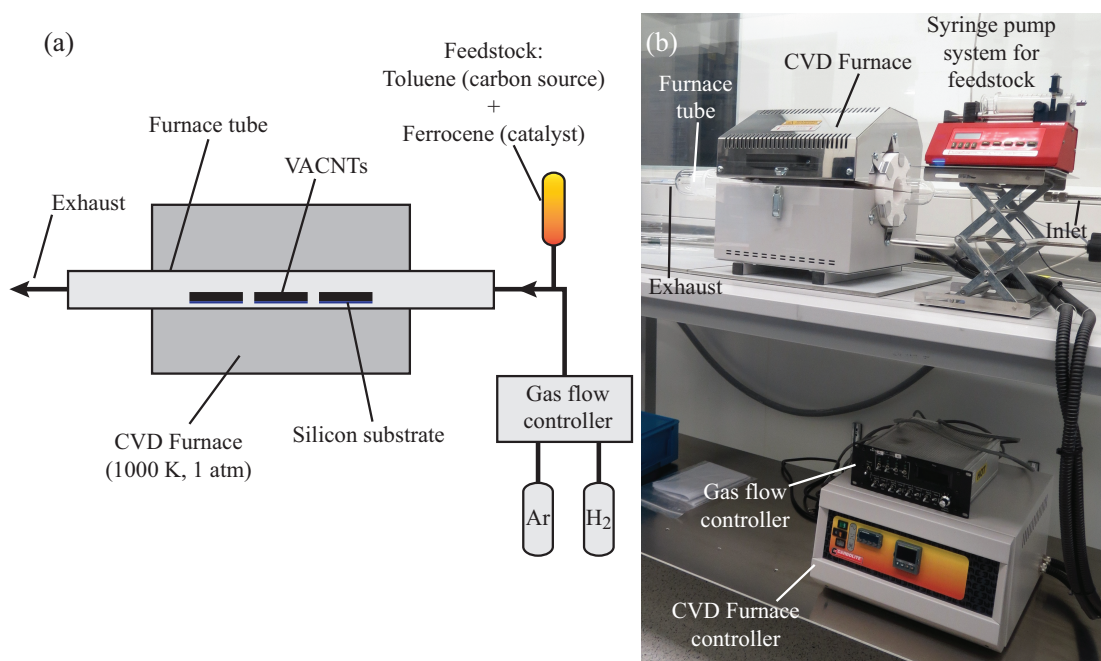### 2.1.1   Floating-catalyst synthesis of carbon nanotube foams

Figure 2.2. (a) A schematic illustration and **(b)** a photograph showing the floating catalyst thermal chemical vapor deposition (tCVD) system used for synthesis of VACNT foams (currently located at the Binnig and Rohrer Nanotechnology Center, IBM Zurich, Switzerland).

Most of the VACNT foams and VACNT structures used in this study were synthesized using a floating-catalyst thermal chemical vapor deposition (tCVD) process. A schematic illustration and a photograph of the floating-catalyst tCVD system are shown in Figure 2.2. As shown in the figure, the tCVD system used for floating catalyst synthesis of VACNTs consists of a CVD furnace with its control system, a horizontal furnace tube, carrier gas supply with mass flow controllers, and a syringe-pump system for feedstock injection.

The feedstock solution of the synthesis consists of the carbon source, toluene ($C_6H_5CH_3$) and the catalyst pre-cursor, ferrocene ($Fe(C_5H_5)_2$), mixed at 0.2 g ml^{-1}. A quartz furnace tube (inner diameter, 50 mm; outer diameter, 55 mm; length 650 mm) is first cleaned well to remove any impurities and then placed horizontally in the tube furnace with a 200 mm heating zone (*Carbolite* product no. *HST12/-/200/E201*; maximum temperature 1200 ^{o}C). Three standard thermally oxidized silicon wafers (each of size ~ 25 mm x 35 mm) with ~1 μm oxide layer are placed inside the heating zone of the furnace tube to facilitate VACNT synthesis as growth substrate. The furnace tube is maintained at 827 ^{o}C and atmospheric pressure throughout the synthesis. The carrier gas, argon (Ar) balanced with 5% hydrogen (H_2), is flown into the furnace tube at steady flow rate of 800 sccm, controlled by the mass flow controllers. The presence of a small amount of hydrogen results in better yield and higher purity of VACNTs (fewer amorphous carbon particles) [42]. The feedstock solution (carbon source and catalyst) is then injected into the carrier gas Ar, at 1 ml min^{-1} using a syringe-pump system (*PumpSystemsInc.* product no. *NE-1000*). Typically 50-60 ml of feedstock solution is used to synthesize VACNT arrays to heights in the order of a millimeter, and the amount is varied if longer/shorter VACNTs are desired. Given such controlled synthesis conditions the VACNTs grow on the silicon substrate in a bottom-up fashion [97,98] and the resultant samples have an average bulk density, 0.27±0.02 gcm^{-3}. Once the synthesis is completed, the furnace is cooled down to below 400 ^{o}C with the Ar gas still flowing and then the samples are taken out of the furnace tube. The standalone VACNT foam samples with 5 mm diameter are cut and extracted from the substrate using a custom-made core drill for mechanical characterizations.
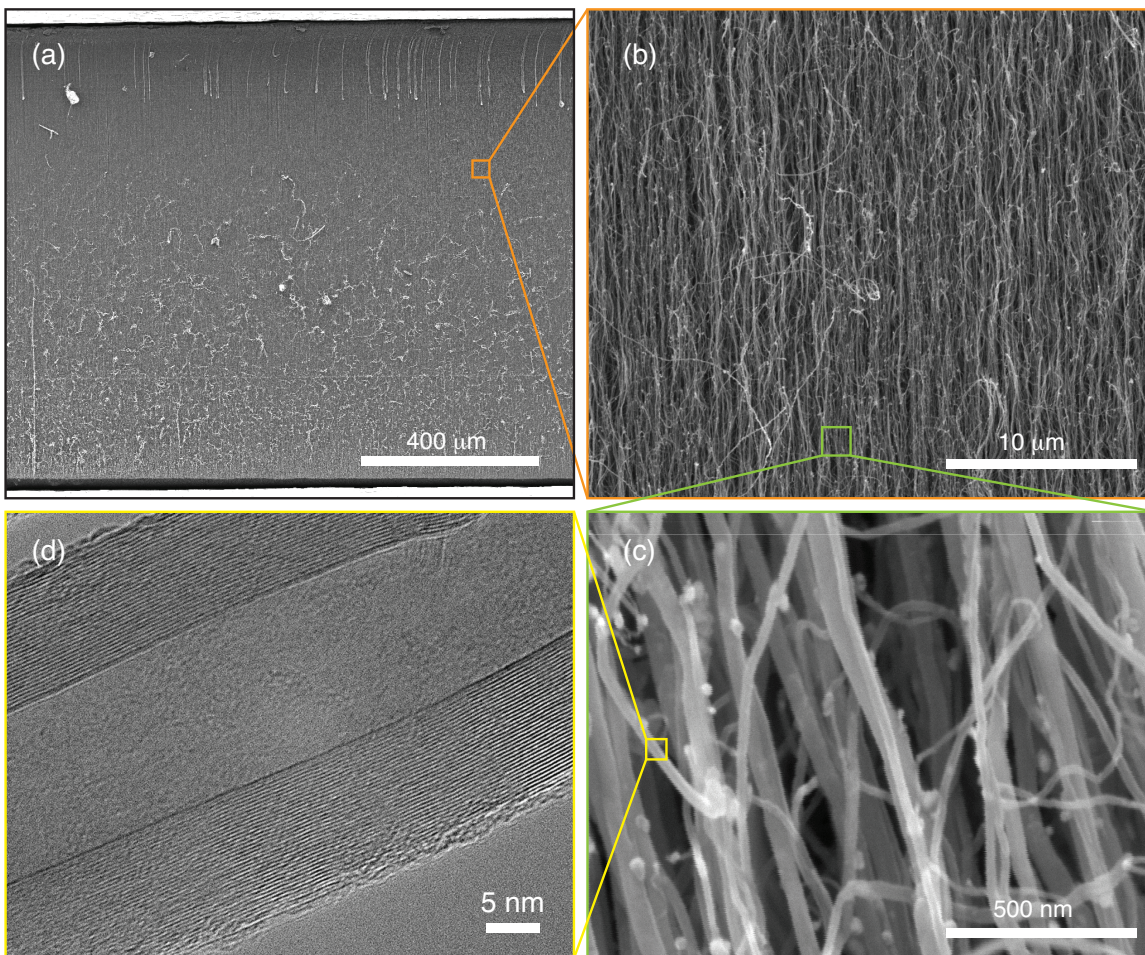
Figure 2.3. Hierarchical fibrous morphology of VACNT foams synthesized using the floating-catalyst tCVD process: **(a)** SEM image of a macroscale VACNT foam, **(b)** SEM image of aligned bundles in mesoscale, **(c)** SEM image of entangled MWCNTs in microscale **(d)** TEM image of a MWCNT with multiple walls forming a concentric cylindrical structure in nanoscale (TEM image is a courtesy of Jordan R. Raney (Caltech)).

VACNT foams synthesized using this tCVD process present a hierarchical fibrous morphology in which bundles of multi-walled carbon nanotubes (MWCNT) are vertically aligned at the mesoscale and form a forest-like system in the micro- and nano-scales. The individual MWCNTs have diameters of 15-70 nm (with an average of ~46 nm) and the number of walls is, on average, ~56 [42]. The number of walls and the morphology of the synthesized forest of VACNTs are tunable by introducing different concentrations of hydrogen during synthesis [42]. Raney et al. have shown that introducing up to 50%

hydrogen into the carrier gas argon can decrease the bulk density by up to ~0.1 g cm^{-3} on average [42]. This decrease in bulk density is related to the reduced diameter of the CNTs, with an average diameter of ~19 nm, and the lower number of walls in the MWCNTs, with an average of ~18. A detailed discussion of the effect of hydrogen on the morphology and the mechanical properties measured in quasistatic compression can be seen in [42].

2.1.2 Fixed-catalyst synthesis of carbon nanotube foams

We used a tCVD system manufactured by *Axitron* for the fixed-catalyst VACNT synthesis. This system consists of a vertical quartz furnace tube with gases flowing from top to bottom while two heater coils at the top and bottom maintain the desired temperature inside the furnace tube. The two heater coils can be controlled independently to produce a temperature gradient, if desired. We have not used any temperature gradients for our VACNT synthesis; however, the effect of temperature gradient on the VACNT growth has been studied previously [28]. It has been reported that the CNT diameter and number of walls can be tailored by utilizing temperature gradients and efficient growth can be achieved above 700 $^{\circ}$C [28]. In our synthesis, the reaction gases pass through the top coil while getting heated up to the temperature of the reaction chamber and then reach the growth substrate. The growth substrates are placed on a horizontal graphite base, right above the bottom heater coil, to facilitate the synthesis.

Compared to floating-catalyst synthesis, the pre-deposited catalyst synthesis requires an additional step of depositing the catalyst on the substrate. We used an electron beam evaporation (*Evatec 501* e-beam evaporator) technique to deposit a thin film of catalyst on the substrate. First, a 20 nm thick aluminum base layer is applied on a 4-inch silicon substrate at a rate of 0.2 nm/s, and then a 2 nm thick Fe-catalyst is deposited at a rate of 0.1 nm/s. The VACNT foams synthesized using this technique were very soft samples that were susceptible to damage during post-synthesis handling. Extracting the VACNTs from substrate as standalone VACNT foams was also not possible. Hence, we diced the 4-inch silicon wafer to 80% of its thickness and into 5 mm x 5 mm grids before depositing the catalyst. This allowed the extraction of samples of controlled size (on substrate) for

mechanical testing, and all the mechanical tests were performed on the samples whilst still attached to their substrates.
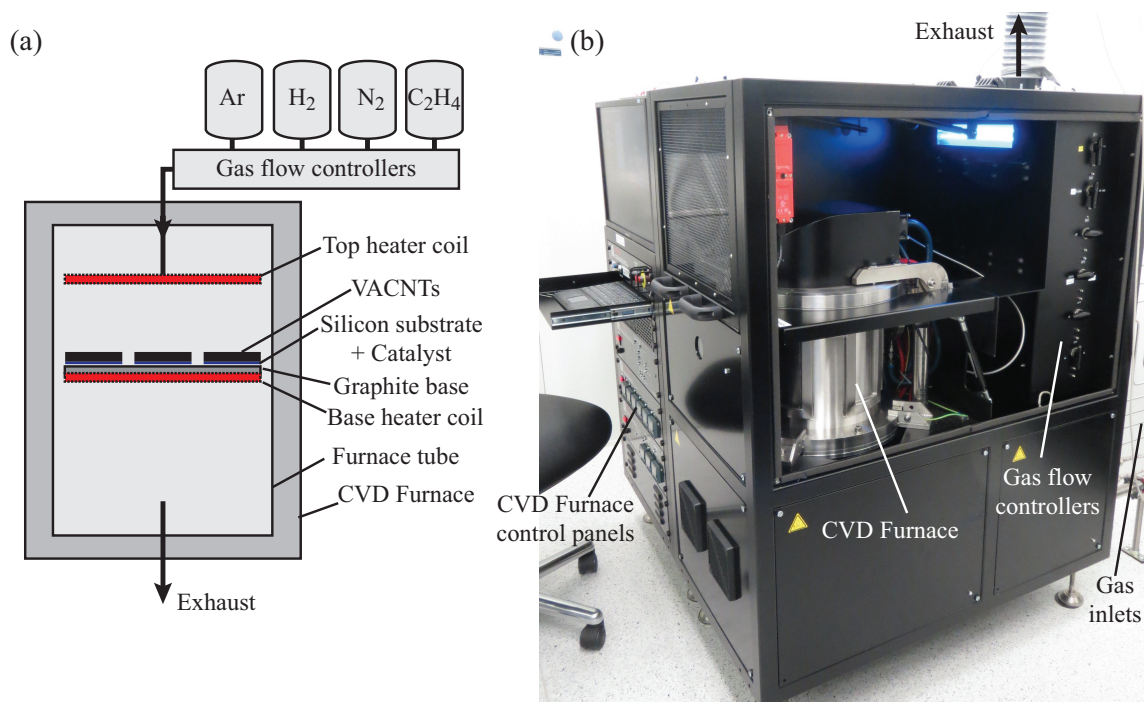

Figure 2.4. (a) A schematic illustration and **(b)** a photograph of the thermal chemical vapor deposition (tCVD) system (*BlackMagic Pro 4" Axitron*, located at the Binnig and Rohrer Nanotechnology Center, IBM Zurich, Switzerland).

Before placing the substrate with fixed-catalyst into the CVD reactor, the reactor is cleaned at 500 $^{\circ}$C for 10 min using oxygen plasma to remove any impurities. The reactor temperature is kept close to 200 $^{\circ}$C to minimize moisture condensation. After substrate placement, the CVD chamber is sealed well and vacuumed to below 0.2 mbar. Then an annealing step is performed by flowing Nitrogen (N_2), Hydrogen (H_2) and Argon (Ar) at 100, 160 and 240 sccm, respectively, and the pressure is raised to 400 mbar. Following 30 minutes of hydrogen annealing at 200 $^{\circ}$C, the temperature is raised to 800 $^{\circ}$C and maintained steady. Then the carbon source, ethylene (C_2H_4), is flown at 120 sccm for the synthesis of VACNTs. Once the synthesis is completed, flows of all the gases are terminated except N_2, and the chamber is cooled down below to 400 $^{\circ}$C in N_2 at 13,000 sccm flow-rate. Once the temperature is decreased to below 400 $^{\circ}$C, N_2 flow is terminated

and the chamber is vacuumed to 0.5 mbar to remove any remains of the reaction gases. Then the chamber is vented to reach atmospheric pressure (1 bar) and the samples are removed from the CVD chamber. The VACNT foams grown in this process are highly sensitive to the chamber conditions and their yield and uniformity are significantly affected by any contaminants present in the chamber. To ensure uniform growth and high yield of VACNTs, the whole chamber is always pre-treated at high temperature, and oxygen plasma assisted cleaning is performed as required.
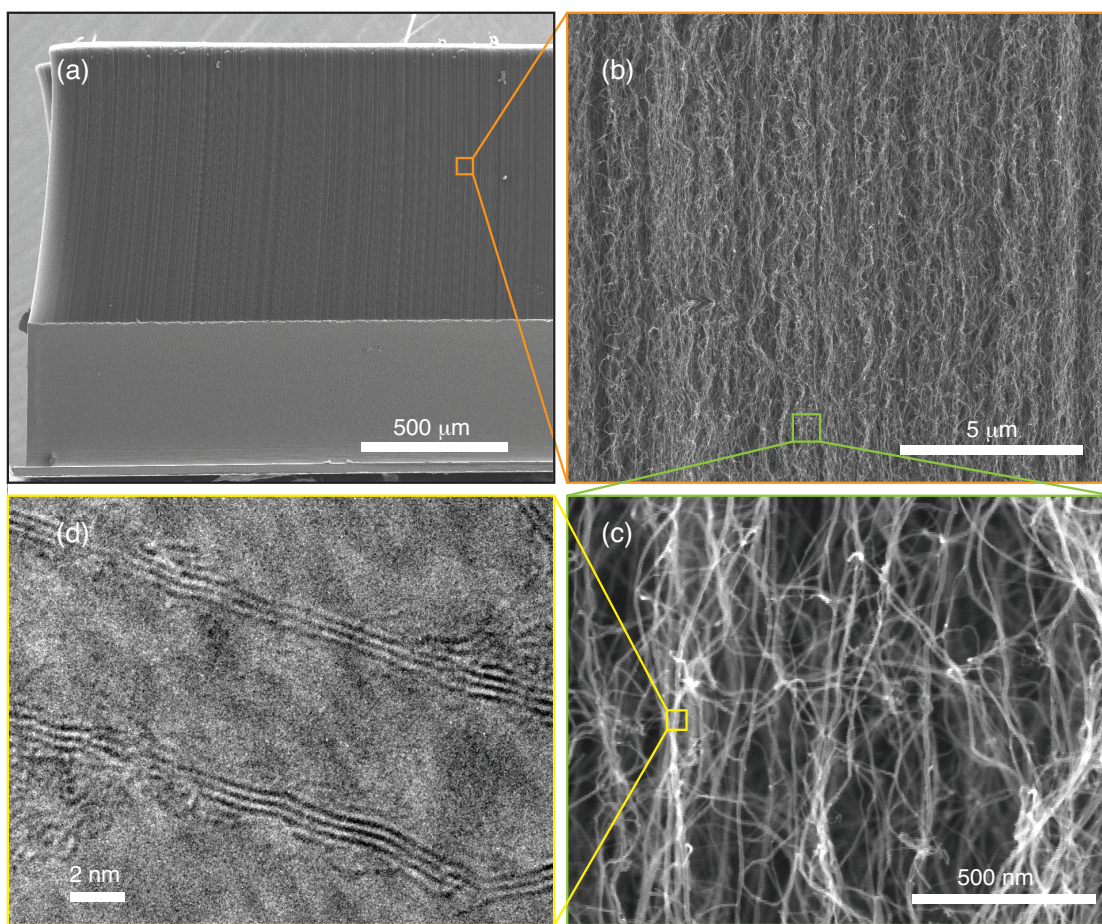

Figure 2.5. Hierarchical fibrous morphology of VACNT foams synthesized using fixed-catalyst tCVD process: **(a)** SEM image of a macroscale VACNT foam on substrate, **(b)** SEM image of aligned bundles in mesoscale, **(c)** SEM image of entangled MWCNTs in microscale **(d)** TEM image of a MWCNT with three walls forming a concentric cylindrical structure in the nanoscale.

The resultant VACNT foams have a hierarchical morphology similar to the VACNT foams synthesized using floating-catalyst tCVD. However, the individual MWCNTs have much smaller diameters of 8.6±1.8 nm on average, and have three to seven walls, as seen in the transmission electron microscope (TEM) images. The bulk samples are grown to a height in the order of a millimeter and have an average bulk density, 0.011 ± 0.0031 g cm^{-3}. After the synthesis, the 5 mm x 5 mm samples with the substrates are extracted along the pre-defined grid lines (defined through substrate dicing) for mechanical characterization.

2.1.3 Synthesis of helical carbon nanotube (HCNT) foams

A floating-catalyst synthesis process similar to the one discussed above in Section 2.1.1, but on a two-stage tCVD reactor, was used to synthesize HCNT foams. The research group of Professor Apparro M. Rao at Clemson University (South Carolina) performed the synthesis, and a brief account on the synthesis is given below. More details on the HCNT morphology and the mechanics of HCNTs are presented in Chapter 4.

HCNT foams are synthesized using a two-stage thermal chemical vapor deposition (CVD) process. The two stages in the CVD reactor—the preheater and the furnace—are maintained at 200 and 700 °C, respectively. The silicon wafers (3cm x 3cm) are then placed in a CVD chamber and heated from room temperature to reaction temperature in the presence of argon (Ar) and hydrogen (H_2) flown at 500 sccm and 100 sccm, respectively. The rate of temperature increase during heating is 15 °C /min. Ferrocene $(Fe(C_5H_5)2)$ and xylene $(C_6H_4(CH_3)_2)$ are used as the catalyst precursor and carbon source, respectively. The indium (In) and tin (Sn) sources (indium isopropoxide and tin isopropoxide) are dissolved in a xylene–ferrocene mixture where the ratio of C:Fe:In:Sn is maintained at 99.16:0.36:0.1:0.38. This feedstock solution is then continuously injected into the quartz tube CVD reactor using syringe pump at an injection rate of 1.5 ml/h after reaching the reaction temperature. Simultaneously, acetylene (C_2H_2) along with Ar carrier gas is passed into the CVD reactor at atmospheric pressure with flow rates 50 sccm and 500 sccm, respectively. Subsequently, after ~ 1 hour of reaction time, the syringe pump and acetylene injection are shut off and the CVD reactor is allowed to cool to room temperature in continued Ar flow. The HCNTs are grown on silicon wafers that

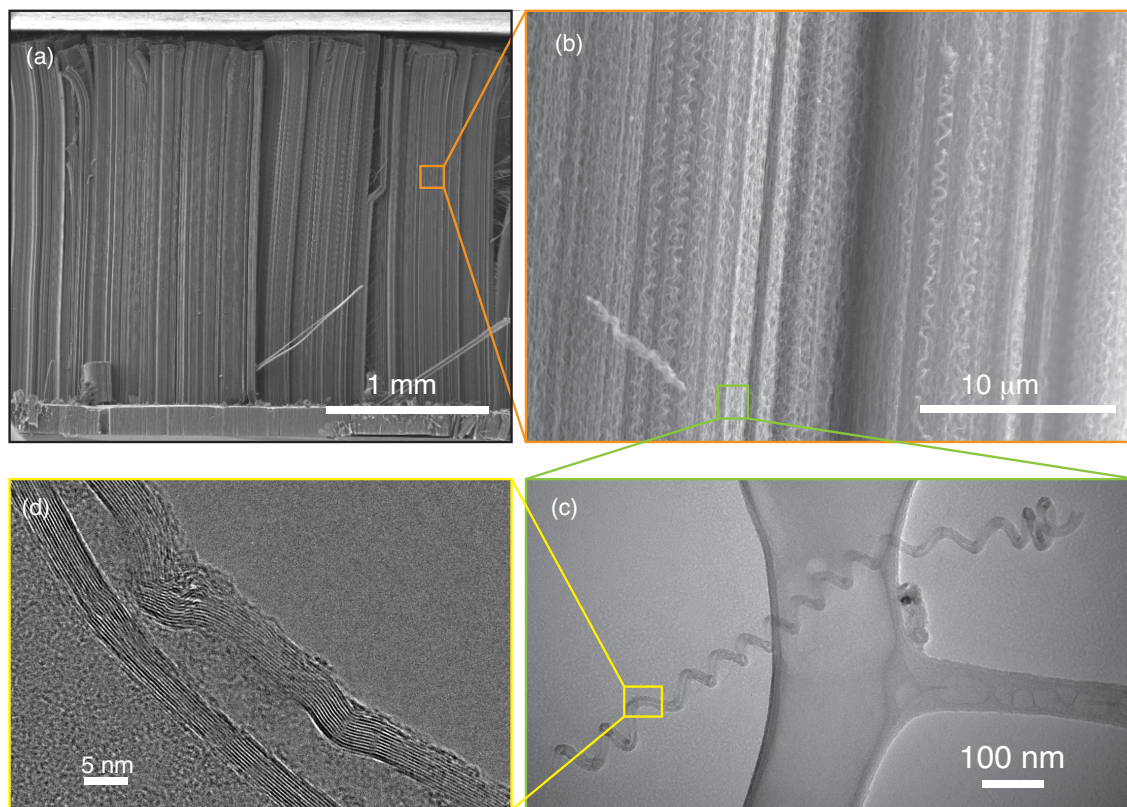are placed inside the furnace tube prior to the synthesis. The resultant HCNT foams have a height of ~ 1 mm.

Figure 2.6. Hierarchical morphology of HCNT foams synthesized using the floating-catalyst tCVD process: **(a)** SEM image of a macroscale HCNT foam on substrate, **(b)** SEM image of aligned bundles of entangled HCNT fibers in mesoscale, **(c)** TEM image of a helical nanocoil in nanoscale **(d)** TEM image of a HCNT fiber showing the multiwall structure in the nanoscale.

HCNT foams have a hierarchical microstructure in which spring-like nanocoils formed by MWCNTs intertwine to form vertically aligned bundles of tubes in the mesoscale. The indium catalyst is known to promote helical coil structure and the non-wetting characteristic of the In catalyst is suggested as the underlying mechanism that leads to HCNT growth [99]. Further details on the vertically aligned HCNT array synthesis can be found in [52].
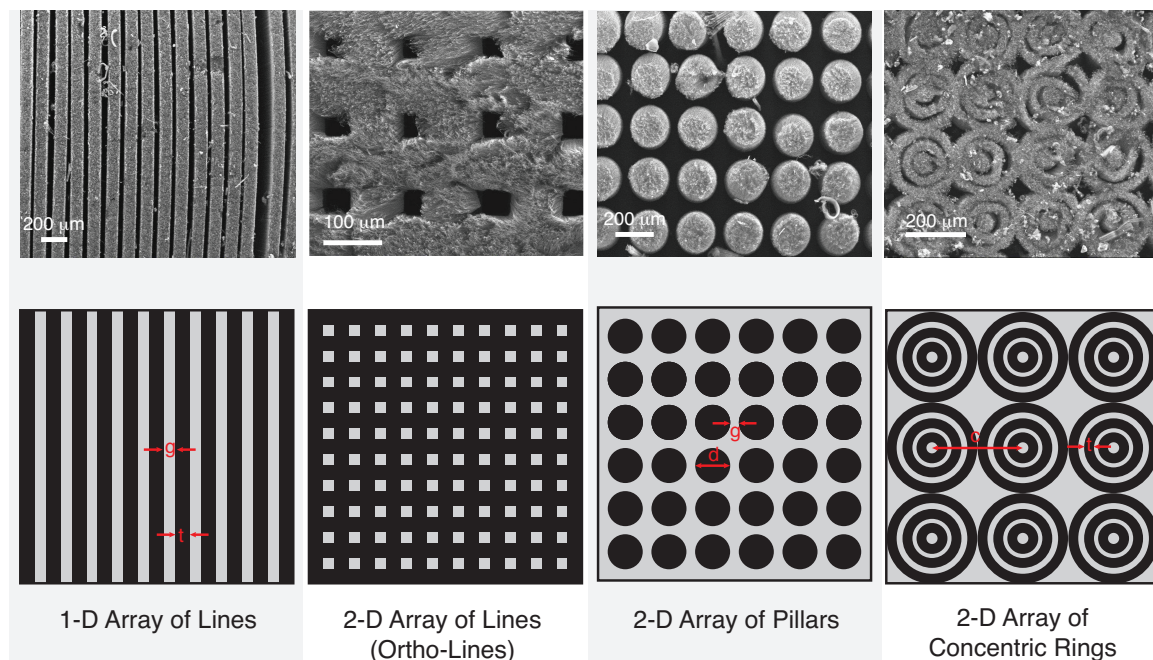
2.1.4 Synthesis of micro-architectured VACNT foams

| 1-D Array of Lines | 2-D Array of Lines (Ortho-Lines) | 2-D Array of Pillars | 2-D Array of Concentric Rings |

Figure 2.7. Schematic top view of the patterns and the SEM images of the micro-architectured VACNT foams.

The micro-architectured VACNT foams were synthesized by Ludovica Lattanzi, a visiting student in our research group from Politecnico di Milano, Italy. They were synthesized on photolithographically patterned silicon wafers by the floating catalyst thermal chemical vapor deposition (tCVD) process described in Section 2.1.1. The method of photolithographic patterning used to pattern the substrates is described below.

The micro-patterns on the substrates are created using photolithographic techniques. The silicon wafer is first dehydrated at 130 °C on a hot plate for 60 s. The Hexamethyldisilazane (HDMS) primer is then deposited by evaporation for 300 s on the dehydrated silicon wafer. After that, the AZ positive photoresist is spin-coated on the substrate, which is then exposed to UV light under a mask with the desired geometry for 3 seconds at 330 W. Then the substrate is immersed into a developer bath and subsequently chromium thin film is evaporated onto its surface using an electron beam evaporator. Finally, the wafer is washed in acetone to remove the undeveloped

photoresist, leaving the chromium thin film where CNT growth was not desired. We used masks with different geometries in 1-D and 2-D arrays to pattern the substrate. The patterns include 1-D arrays of lines with varying gaps, 2-D arrays of lines (orthogonal lines), circles with varying gaps and diameters, and 2-D arrays of concentric rings. The VACNTs are then grown on the defined pattern area forming three dimensional micro-architectured VACNT structures.

2.1.5 Toxicity of CNTs and safety precautions

CNTs are considered toxic and are generally handled with care according to nanoparticle safety guidelines. Particularly, due to their high aspect ratio, CNTs are often compared to asbestos fibers and their harmful effects on health [100]. CNTs injected into mice's stomach cavities have been shown to cause inflammation suggesting that they may pose long term health effects [101]. In contrast, another study found that the CNTs, unlike asbestos fibers, did not cause immediate cell death when injected in human lung and immune cells [102]. Long-term health effects, however, may take several decades to unfold and in most cases of synthesis and handling, general nanoparticle toxicity is assumed.

We synthesized the VACNT samples in closed environments inside a laboratory fume hood. Currently both the home-built floating-catalyst synthesis system and the *Axitron BlackMagic* fixed-catalyst synthesis system are located in the clean room of Binnig and Rohrer Nanotechnology Center, IBM Zurich, Switzerland. The whole synthesis and post-synthesis cleaning procedure is established with care to avoid any exposure to nanoparticles either through inhalation or skin contact. Post-synthesis sample preparation for mechanical testing is performed inside a glove box with no direct exposure to nanoparticles. When performing impact experiments, an exhaust hood is placed directly above the experimental setup to safely collect any fragmented particles that may become airborne. All samples are stored in closed containers reducing any risk of nanoparticles becoming airborne.

2.2 Morphological characterizations using synchrotron x-ray scattering and mass attenuation

The morphology of the VACNT foam and HCNT foam samples were characterized using synchrotron x-ray scattering and mass attenuation measurements at the Advanced Light Source of the Lawrence Berkeley National Laboratory. Dr. Eric R. Meshot, a post-doctoral scholar at the Lawrence Livermore National Laboratory, performed the synchrotron x-ray measurements and provided the morphology details for our samples. The measurements were performed to nondestructively characterize the morphology along the height of the samples, and provided information on intrinsic mass density gradients, alignment of CNT fibers, and diameter distributions. A brief, general overview of these experiments and data reduction methods is given below. More details on experiments and the data specific to different samples are provided in Chapter 3 and Chapter 4 of the dissertation.
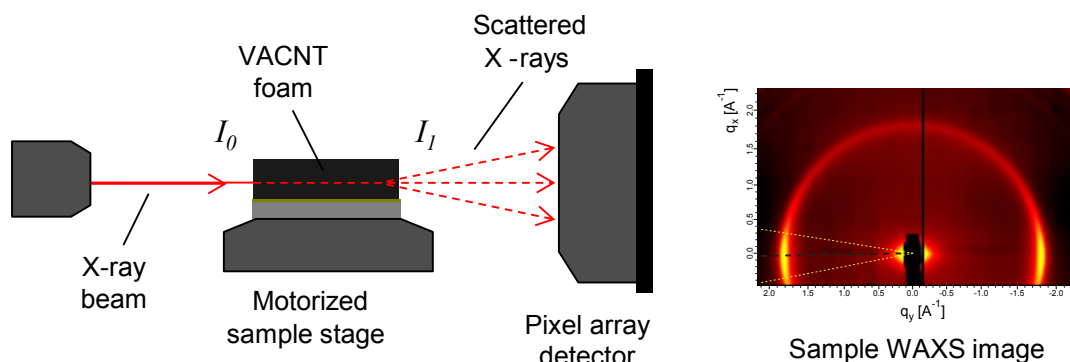

Figure 2.8. Schematic side view of the experimental setup for X-ray characterization with a representative wide-angle x-ray scattering (WAXS) image collected from our VACNT foams. The x-z-α stage enables spatial mapping and alignment of the CNT to the X-ray beam, and the scattered X-rays are collected on a Pilatus 1M pixel detector.

A beam energy of 10 keV was selected with a Mo/B_4C double multilayer monochromator, and the height of the beam-spot was less than 300 μm at the sample with a measured flux of 10^{12} photons sec^{-1}. The CNT foam sample was mounted on a motorized stage that

enabled 1) tilt alignment to make the sample's Si substrate parallel to the X-ray beam as well as 2) spatial mapping of the structural characteristics of the sample along its height.

We monitored the X-ray intensity upstream (I_0) and downstream (I_1) of the sample by measuring ion current at the locations denoted in the schematic. These values were used to calculate the mass density of the sample based on the Beer-Lambert law [103],

$$\rho_{\text{CNT}} = \frac{\ln\left(I_0/I_1\right)}{t\left(\mu/\rho\right)}, \tag{2.1}$$

where ρ_{CNT} is the CNT foam's volumetric mass density, t is the path-length through the CNT foam, and (μ/ρ) is the mass attenuation coefficient. Values for (μ/ρ) are tabulated by the National Institute of Standards and Technology (NIST) as a function of element and X-ray energy.

In the case of VACNT foams, we used a weighted average between C and Fe (equation 2.2), because our floating-catalyst synthesis of VACNT foams deposits small quantities of Fe, which we measured to be approximately 5% by energy-dispersive X-ray spectroscopy (EDX) in scanning electron microscope (SEM).

$$\left(\mu/\rho\right) = (1 - w)\left(\mu/\rho\right)_{\text{C}} + w\left(\mu/\rho\right)_{\text{Fe}}, \tag{2.2}$$

where w is the weight fraction of Fe.

In addition to measuring the X-ray attenuation, we also quantified the average CNT alignment from the anisotropy of wide-angle X-ray scattering (WAXS) or small-angle X-ray (SAXS) patterns. Using the distribution of scattered intensity about the azimuthal angle φ, we calculated the Herman's orientation factor [104,105],

$$f = \frac{1}{2}\left(3\langle\cos^2\varphi\rangle - 1\right). \tag{2.3}$$

Here, f equals 1 for perfectly aligned CNTs and 0 for random order (no alignment), and

$$\langle\cos^2\varphi\rangle = \frac{\int_0^{\pi/2} d\varphi\, I(\varphi)\sin\varphi\cos^2\varphi}{\int_0^{\pi/2} d\varphi\, I(\varphi)\sin\varphi}. \tag{2.4}$$
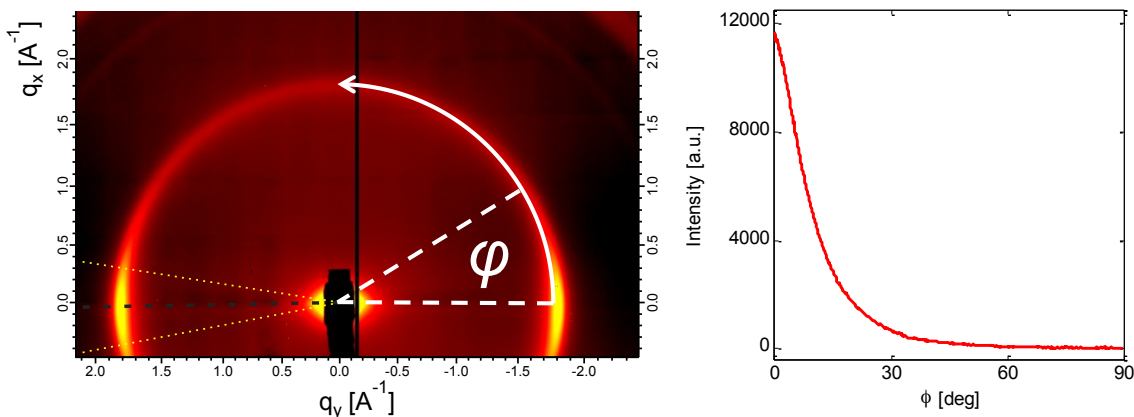
Figure 2.9. Schematic illustration demonstrates the azimuthal integration we perform on WAXS images to extract the Herman's orientation factor. The annulus of integration is defined by ±5 pixels from the diffraction peak located at q = 1.8 Å^{-1}, which corresponds to scattering from the concentric shells of multiwall CNTs.

2.3   Quasistatic mechanical characterization

We used a commercial testing system, *Instron Electro Pulse E3000,* for mechanical characterization in quasistatic compression. It has been used for performing strain-controlled quasistatic compression experiments with multiple loading-unloading cycles and has a displacement resolution of 1 μm. Compression tests are performed typically in the low strain-rate regime between 10^{-4} and 10^{-1} s^{-1}. Two load cells with maximum load ranges of up to 250 N and 3000 N are used for the compression tests, depending on the load sensitivity of the samples tested. For example, most of the experiments on the VACNT foams synthesized by the floating-catalyst tCVD process required a 3000 N load cell for compression tests up to 80% strain, whereas the VACNT foams synthesized using the fixed-catalyst tCVD process required a 250 N load cell to capture the stress-strain response with less noise at low-stress levels. From direct measurements of forces and displacements during cyclic compression, the quasistatic stress-strain response is obtained by normalizing the force by sample cross-sectional area, and the displacement by sample thickness. Once the stress-strain response is known, several mechanical properties such as loading modulus, unloading modulus, compressive strength, strain recovery and hysteretic energy dissipation

can be calculated. To understand the microscale deformation mechanisms in quasistatic compression, *in-situ* microscopy is often used simultaneously with the mechanical testing.

2.4 Dynamic mechanical characterization[1]

In this section, we describe an experimental technique for the study of dynamic behavior of complex soft materials, based on high-speed microscopic imaging and direct measurements of dynamic forces and deformations. The setup includes high sensitivity dynamic displacement measurements based on geometric moiré interferometry and high-speed imaging for *in-situ*, full-field visualization of the complex micro-scale dynamic deformations. The method allows the extraction of dynamic stress–strain profiles both from the moiré interferometry and from the high-speed microscopic imaging. We discuss the advantages of using these two complementing components concurrently. We use this technique to study the dynamic response of vertically aligned carbon nanotube foams subjected to impact loadings at variable deformation rates. The same technique can be used to study other micro-structured materials and complex hierarchical structures.

2.4.1 Background on dynamic characterization of soft, complex materials

Complex materials have hierarchically organized constituents that are either self-assembled naturally (e.g. natural and biological materials such as wood, bone, teeth and seashells) or engineered to have constituents ranging from nanometers to millimeters in size (e.g. micro and nano structured metamaterials, vertically aligned carbon nanotube (VACNT) structures, etc.) [106]. Biological complex materials are characterized by optimal mechanical properties that can combine strength, stiffness and toughness, and can serve as models for the design of synthetic composites [3,107]. Synthetic complex materials outperform conventional materials by exhibiting exceptional multi-functional properties (for example, superior thermoelectric, piezoelectric and optoacoustic properties) and can achieve effective mechanical properties not found in natural materials (for example, negative elastic moduli, phononic band gaps, and high specific energy

---

[1]This section is adapted from our paper authored by R. Thevamaran and C. Daraio [169]. RT and CD designed the study. RT designed and built the experimental setup, synthesized samples, performed the experiments and wrote the manuscript with the support of CD. Both authors contributed to the interpretation of the data and writing of the manuscript.

absorptions) [2,106–109]. Soft complex materials undergo large finite deformations with shape changes when subjected to an external stress field and may exhibit distinct deformation characteristics at different length and time scales [110]. Understanding the behavior of complex soft materials in a broad range of strain-rates from 10^{-8} to 10^{8} s^{-1} is of great interest to material scientists and engineers to: (i) understand the fundamental mechanisms that govern the mechanics and the resultant material behavior; (ii) synthesize novel materials with physical properties that can be tailored for specific applications.

At very low rates (10^{-8}-10^{-6} s^{-1}), creep and stress relaxation experiments subjected to prolonged loading conditions have been used to study the viscoelastic and long-term behavior [60,111]. At quasi-static rates (10^{-4}-10^{0} s^{-1}) tensile, compression, indentation and shear experiments have been adapted to understand complex deformation responses of hierarchical structured materials [112]. At higher rates, dynamic mechanical analysis (DMA) is a commonly used technique to obtain the material parameters such as storage and loss modulus [65]. Nonetheless, DMA has been limited to small strain amplitudes and has not been successful in characterizing inhomogeneous materials with intrinsic gradients in functional properties. At yet higher rates, drop ball impact testing [53], projectile impact experiments [113] and shock wave excitation [108] have been used to study the rate-dependent material behaviors. For each experimental technique used, appropriate force and displacement measurement systems have been designed and improved. The most common experimental methods and detection systems used to test materials at different rates of deformations [114–116] are summarized in Figure 2.10.

Experimental method	Strain-rate (s^{-1})	Displacement sensing: example optical techniques
	10^{-8}	
Creep, Relaxation experiments		Time-lapse photography
	10^{-4}	
Quasistatic Compression, Tension, Shear experiments, Nano-indentation		Videography, In-situ scanning electron microscopy, Digital image correlation, Interferometry techniques
	10^{0}	
Dynamic mechanical analysis, Specialized instrumentations		High-speed imaging, Interferometry techniques
	10^{2}	
Drop-weight impact Hopkinson pressure bar		High-speed imaging, Digital image correlation Interferometry techniques
	10^{4}	
Plate impact experiments		Ultra-high-speed imaging, Digital image correlation Interferometry techniques
	10^{8}	

Figure 2.10. Overview of mechanical testing techniques and of the relevant optical measurements.

Non-contact, optical visualization methods have been the most widely adopted and rapidly evolving techniques for *in-situ* imaging and quantitative displacement measurements. Recent advancements in high-speed imaging and digital image correlation methods [117–119] enabled the mechanical, damage and fracture characterization of macroscopic complex materials, at various rates of deformations [120–122]. At smaller scales, quasi-static nano-indentation experiments performed inside a scanning electron microscope (SEM) have been used to visualize and characterize the localized microscale deformation [123]. Optical interferometry techniques, such as moiré interferometry, speckle interferometry, holographic interferometry, and shearing interferometry have been widely used for non-contact dynamic displacement measurements [114].

Despite all the advances in experimental testing and measurement techniques, the characterization of the dynamic behavior of soft complex materials remains challenging. This is due to their hierarchical microstructure, which requires the characterization of deformation phenomena occurring at both micro- and macro-scales. In addition, the bulk material behaviors of these samples are affected by the presence of large three-dimensional deformations and local effects arising from defects and intrinsic functional property gradients. In this article, we present an experimental technique to characterize

the dynamic response of complex soft materials. The technique measures the global dynamic constitutive response, using dynamic force sensors and non-contact optical interferometry (moiré). This allows for the characterization of the samples' large deformations. The local dynamic effects, occurring at the micro-scale, are captured by *in-situ* visualization using high-speed microscopic imaging. The ability to acquire microscopic images also facilitates the characterization of thin samples. We target dynamic characterization at nominal strain rates ranging from 10^2-10^4 s^{-1}.

In the following sections, we provide a detailed account of the experimental setup (Section 2.4.2-6), VACNT specimen fabrication (Section 2.4.7), data reduction methodologies (Section 2.4.8), comparison of the dynamic behavior of VACNT foams obtained independently from the two displacement measurement components of the experimental setup: geometric moiré interferometry and high-speed microscopic imaging (Section 2.4.9) and a discussion on the observed dynamic behavior of VACNT foams (Section 2.4.10).

2.4.2 Experimental setup

The dynamic testing apparatus (Figure 2.11 (a), (d)) described here has four main components: (i) a striker impact system, (ii) a dynamic force sensor, (iii) a dynamic displacement transducer, and (iv) a high-speed camera with a microscopic lens for visual observation and characterization of the deformation. The details of each of these components are described in the following sections.
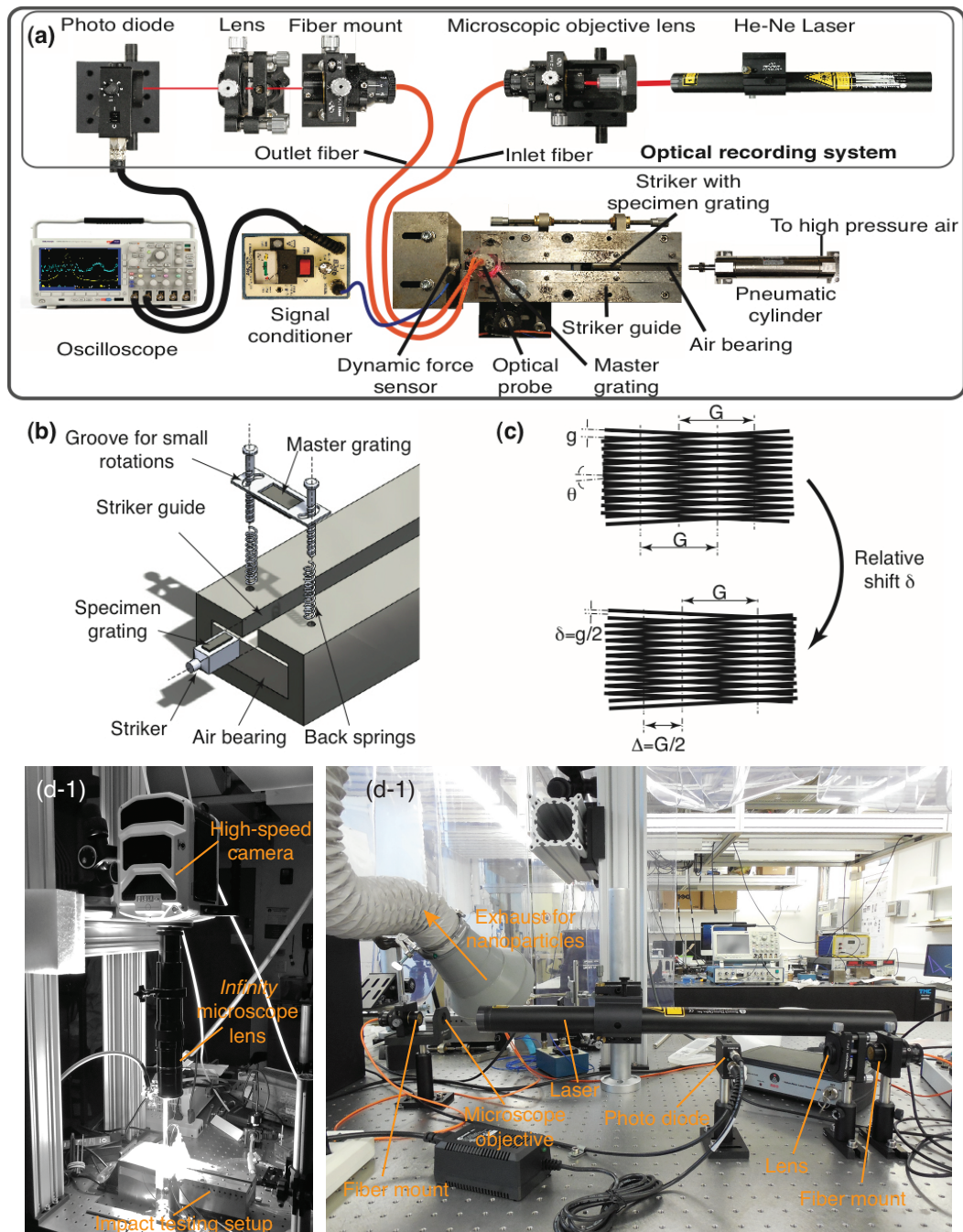
Figure 2.11. Geometric moiré interferometry-based dynamic testing setup: **(a)** experimental set up, **(b)** schematic of geometric moiré implementation on striker guide assembly, **(c)** schematic of geometric moiré fringe formation and fringe shift, and **(d)** photographs showing the high-speed microscope mounted on the experimental setup and the optical recording system for the moiré interferometry.

2.4.3 Striker impact system

The striker impact system consists of a flat-plunge striker, a frictionless striker guide and a pneumatic cylinder to launch the striker on the guide. We use a flat plunge striker made of *Delrin*® acetal homopolymer as the loading apparatus. The striker material was chosen to have adequate stiffness to accommodate no or minimal deformation compared to the material being tested. The *Delrin*® acetal homopolymer has two-orders-of-magnitude higher modulus than the modulus of VACNT foams. Its material properties are: density, 1.41 gcm^{-3}, tensile and compressive modulus, 3.10 GPa, compressive strength, 110 MPa, and Rockwell hardness, R122 [124]. The main body of the striker is 28.5 mm long and has a square cross-section (side length=12.70 mm). It has a cylindrical plunge (length=diameter=6.35 mm) with a flat face as the loading front. The flat loading front was chosen to provide uniaxial planar impacts to the specimen. It should be noted that albeit indentation is being used as an indirect method to obtain material properties [125,126], the interaction of sharp indenter tips with structured materials with complex microstructure is not well understood [126,127]. However, if a dynamic indentation experiment is desired, the loading front of the striker in our system can be modified to accommodate spherical indenters or sharp indenter shapes, as in Vickers and Berkovich [128]. The square cross-section of the striker body was selected to prevent any rotation that might significantly impair the quality of the moiré fringes.

A stainless steel double-acting pneumatic cylinder (*McMaster-Carr*, with bore 26.98 mm, and stroke 38.10 mm) was used to launch the striker on a frictionless striker guide. An air regulator coupled with a pressure gauge varied the pressure in the pneumatic cylinder from 10-60 psi (68.9–414 kPa) to control the striker launching speed from 1–6 ms^{-1}. The striker guide was designed to propel the striker straight to a travel distance of 200 mm. A spacing of ~10 μm was left between the striker and the confining guide walls to reduce friction. In addition, a ~5 μm thin layer of air was introduced between the striker and the base of the guide using flat rectangular air-bearings to facilitate frictionless traveling of striker. The air bearing (*Newway*®) is made of a micro-porous carbon medium and supplied with high-pressure air to form the thin layer of air. This design of the frictionless

striker guide dramatically enhanced the repeatability of the striker's impact velocities compared to conventional low-friction material assemblies.

2.4.4   Force sensor

We used *PCB Piezotronics Quartz ICP*® impact force sensors (model 200B02 and 200B03) for measuring the transient signals during the impacts. Quartz transducers are desirable for dynamic applications due to the high natural resonant frequency of quarts (> 1 MHz). Similar transducers have been used in several other dynamic testing systems [72,129,130]. The discharge time constants (t) of the sensors used in our experiments are t>500 s for the 200B02 [131] and t>2000 s for the 200B03 [132], which are well above the loading-unloading time of our experiments (~1 ms). These sensors have positive polarity for compression, they have sensitivities of 11241 mV/kN (200B02) and 2248.2 mV/kN (200B03) and can operate up to 444.8 N (200B02) and 2224 N (200B03) with high linearity [131,132]. The *ICP*® force sensors incorporate a built-in amplifier to convert the high impedance charge output to a low impedance signal that is not affected by triboelectric cable noise or contaminants before recording. We conditioned the voltage signal from the dynamic force sensors and amplified it (when required) using an *ICP*® sensor signal conditioner (*PCB Piezotronics* model: 480E09; gain x1, x10, x100) connected to the force sensor by a low-noise coaxial cable (*PCB Piezotronics* model: 003C05). The *Tektronix DPO3034* oscilloscope recorded the output signal from the signal conditioner.

The force sensor was mounted firmly on a rigid stainless steel block with heavy mass according to the specifications provided by *PCB Piezotronics*. We attached the specimen to the striker and let it directly impact the force sensor. For the impact velocity ranges considered (from 1 to 6 m s^{-1}), the force-response time during impact was much larger than the time taken to equilibrate stresses. This implies that the dynamic force measured by the force sensor represents equilibrated stresses. Equilibration of axial stress is essential to ensure that the measured stress represents the average stress in the specimen. Davies and Hunter [133] estimated that the stress equilibration requires three reverberations of the loading wave in the specimen. We estimate this to amount to ~30 μs

in our experiments. This is a conservative estimate using the quasistatically measured modulus of ~10 MPa for a representative VACNT foam with ~0.25 g cm^{-3} density. The longitudinal wave velocity estimated thereby is ~200 m s^{-1} and it will take ~10 μs for one reverberation in a sample of thickness ~1mm. Song and Chen [134] showed that for a soft material, the specimen thickness has a profound effect on establishing stress equilibrium—higher the thickness, longer the initial non-equilibrium stress duration is. In addition, they showed that the high loading rate too has an effect on stress equilibrium, but it is less pronounced compared to that of the thickness of the specimen. The stress equilibration is a critical design consideration for very high loading-rate experiments, like Kolsky split-Hopkinson bar tests, particularly with higher specimen thicknesses; but has low significance in relatively long duration (~1 ms) loading-unloading experiments with moderate loading-rates and thinner specimens (~1 mm).

2.4.5   Dynamic displacement transducer

Accurate dynamic displacement measurement in soft, hierarchical and micro-structured samples is a challenging task that requires the development of an ad-hoc measurement system. The complex microstructure and the small characteristic size of the samples make conventional optical techniques unsuitable, due to the current resolution limits of high-speed cameras and the need for powerful illumination sources. The setup we developed includes a dynamic displacement measurement system capable of capturing micro-scale deformation during impact loadings. The measurement system uses high sensitivity geometric moiré fringes to amplify the microscopic dynamic displacements. Among all the different types of moiré techniques, geometric moiré is one of the simplest to implement. The technique relies on the superposition of two identical line-gratings with a small relative angle of rotation to create a geometric amplification of displacement that can be used for high sensitivity measurements [135–138]. Geometric moiré interferometry was also used in dynamic indentation experiments to study the rate-sensitivity of oxygen-free high-conductivity (OFHC) copper [129]. Geometric moiré fringes are produced by the interference of two identical line gratings (master and specimen gratings) superimposed with a very small relative angle of rotation [135] (see Figure 2.11 (b) and (c)). In most applications of geometric moiré, the master grating is

attached to the experimental fixture and the specimen grating is attached to the sample [135]. The moiré fringes produced this way have a pitch, G, that is related to the pitch of the gratings, g, through a purely geometric relationship [135]:

$$G = \frac{g}{\theta} \, ,$$ (2.4)

where θ is the small relative angle of rotation. The pitch of the grating is the center-to-center spacing between two neighboring dark lines (or white lines), and the half-pitch is the center-to-center spacing between two adjacent dark and white lines. When one grating is displaced by an amount δ relative to its pair, the resulting moiré fringes move to a new position by Δ given by [135]:

$$\Delta = \delta \left(\frac{G}{g} \right) \, ,$$ (2.5)

where $\left(\frac{G}{g} \right)$ is the amplification factor. Hence, this technique can be interpreted as a displacement amplifier that can be used to sense micro-scale displacements. For example, a grating pair at a 2^0 relative angle of rotation amplifies the displacement by nearly a factor of 30.

We implement this technique as follows: the master grating is mounted stationary on the striker guide and the specimen grating is rigidly attached to the striker using a 5 minute epoxy. The specimen grating was attached on the striker, and not on the samples directly, because of the samples' small size and their complex, large deformations under impact. The rigid-body translation of the striker (and attached specimen grating) relative to the stationary master grating produces the shift in the geometric moiré fringes. When the striker is in contact with the sample, the shift in the moiré fringes measures the dynamic deformation of the specimen. The master grating was mounted on the striker guide with back-loaded spring supports as shown in Figure 2.11 (b). This arrangement provides the flexibility to tune the moiré fringe amplification factor by varying the relative angle between the specimen and master gratings.

The gratings used have an identical Ronchi ruling frequency of 40 cycles/mm resulting in a pitch g= 25 μm. The nominal sensitivity of the geometric moiré technique is equal to the pitch of its grating (which corresponds to peak-to-peak distance of the intensity modulation of the moiré fringes). However, we were able to measure displacements at 6.25 μm (quarter-pitch) resolution through data reduction as explained in Sec. 2.4.8. Both the specimen grating (reflective) and the master grating (transparent) were produced by *Applied Images Inc*. The reflective specimen grating was created by first coating a glass substrate with a specular-reflective thin layer of aluminum and then printing precise blue-chrome Ronchi rulings using a semiconductor pattern generator device. Similarly, the transparent grating was produced by patterning blue-chrome lines on a transparent glass substrate. During measurement, the focused laser light from the optical probe passes through the transparent master grating, reflects on the reflective specimen grating and passes again through the transparent grating before being recollected back into the optical probe. The resulting multiplicative intensity, *I*, of the emergent light becomes [135]:

$$I = I_0 \big(T(x,y) \big)^2 R(x,y) , \qquad (2.6)$$

where *R* is the reflectance at each *(x, y)* point of the reflective grating and *T* is the transmission at each *(x, y)* point of the transparent grating. Even though the best multiplicative moiré pattern is obtained when the two gratings are in contact, no deterioration of the pattern is noticeable when the gap between the two gratings is much smaller than g^2/λ, where λ is the wavelength of light and g is the pitch of the gratings [135]. If a red-laser light source (λ=632.8 nm) is used on a grating pair with 25 μm pitch, the gap between the specimen and master gratings should be smaller than 1 mm to produce moiré fringes of sufficient quality for measurements. A relatively large gap is essential during impact experiments, to ensure no damage to the gratings. This becomes a limiting factor in increasing the grating frequency and the related displacement resolution.

The optical system (Figure 2.11) that is used to produce coherent light and record the intensity modulation of the geometric moiré fringe shift has several optical components (the essential design parameters are shown within parentheses): a coherent light source (He-Ne Laser; with a wavelength of 632.8 nm; power 21 mW); an objective lens to focus

the laser light into the inlet fiber; an inlet fiber (with a 50 μm core diameter) that directs the light to the optical probe; an optical probe with two internal miniature lenses (5 mm field depth; 30 mm probe to specimen distance; and a focused spot size on the specimen with a 600 μm diameter; numerical aperture 0.15) to focus the light onto the grating and recollect the emergent light from the grating; outlet fiber (core diameter of 300 μm) that transports the collected emergent light to photo detector; an achromatic lens to focus the light from the outlet fiber onto the photo detector; Si switchable gain photo detector (wavelengths between 350-1100 nm; 17 MHz bandwidth; detection area of 13 mm^2) to detect the light intensity from the optical probe and convert into voltage signal; and an oscilloscope (*Tektronix DPO3034*; analog bandwidth, 300 MHz; sample rate, 2.5 GS s^{-1}; record length, 5 million points) to record the signal received by the photo detector. In addition, several optomechanics components such as multimode fiber couplers, linear stages, lens mounts, laser mount, optical posts, post holders and mounting bases are used in the setup. A photo detector with fine rise-time was selected in order to record the light intensity modulation. For an impact velocity of 5 m s^{-1} and a grating pitch, g, of 25 μm, the time for the dark-bright intensity transition (corresponding to a half-pitch movement) is 2.5 μs. We selected a photo detector with rise time ~60 ns to have enough frequency response to record the moiré fringe shifts. It should be noted that a non-coherent, high intensity, white light source with narrow beam size can be used in place of a coherent laser light source for grating frequencies up to 40 cycles mm^{-1}. In white light illumination conditions, when the grating frequency increases beyond 40 cycles mm^{-1}, the contrasts of the recorded intensity modulations decrease below the noise level and the sensitivity of the moiré setup is not sufficient for data acquisition. The use of a coherent light source improves the fringe contrast and can be used to achieve higher measurement resolution [114].

2.4.6 High-speed microscopic imaging

We use a *Vision Research*'s *Phantom V1610* high-speed camera coupled to a microscopic lens (*Infinity* long-distance microscope system model *K2/SC*) to observe and characterize dynamic deformations (Figure 2.11 (d-1)). The camera has a *CMOS* (35.8 mm x 22.4 mm) sensor with 1280 x 800 pixels maximum spatial resolution and operates at an up to 1

million frames-per-second (fps) frame-rate (with a temporal resolution of 1 μs). A *Karl Storz Xenon Nova 300* high-intensity cold light lamp (which includes a 300 Watt Xenon lamp) connected to a *Karl Storz* liquid light guide cable was used to illuminate the specimen. The light sensitivity of the camera to low-intensity reflected light from our black samples proved to be a limitation in reaching high temporal resolutions (i.e., high frame-rates). We operate the camera at a frame rate of ~150,000 fps, at a resolution of 128 x 256 pixels, focused on a physical window of ~ 1.8 mm x 3.5 mm. *Phantom Cine View 2.14* software is used to control the camera. The camera is synchronized with the rest of the experimental setup and its acquisition is triggered by the trigger-signal from the oscilloscope. *Image Systems*'s *TEMA Motion Analysis* software was used to analyze the image sequence. This software is capable of analyzing the image sequence using a digital image point correlation algorithm with an accuracy of 1 pixel. The high-speed image sequence provides information that enables us to understand the complex dynamic deformation of the VACNT foams that cannot be observed with the geometric moiré interferometry alone.

2.4.7   Test sample (VACNT foams) fabrication

We study the dynamic response of VACNT foams using the described testing system. To synthesize the CNT foams we use a floating catalyst thermal chemical deposition (tCVD) process [42]. The carbon source (toluene), and catalyst pre-cursor (ferrocene) mixed at 0.2 g ml^{-1} were injected at 1 ml min^{-1} into the carrier gas (argon) flowing at 800 sccm. Oxidized silicon substrates, placed inside a 15 cm heating zone of a quartz furnace tube, were used as growth substrates. The furnace tube was maintained at 827 ^{0}C and atmospheric pressure throughout the synthesis. VACNT foams synthesized using this tCVD process have been shown to present a hierarchical fibrous morphology ([42] and Figure 2.12) in which bundles of multi-walled carbon nanotubes (MWCNT) are vertically aligned at the meso-scale and form a forest-like system in the micro- and nano–scales. The physical properties of the samples synthesized for this work are provided in Table 2.1.
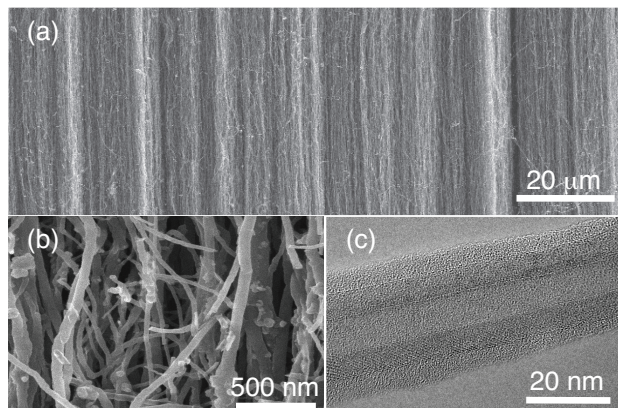
Figure 2.12. Hierarchical morphology of VACNT foams: **(a)** SEM image of the vertically aligned bundles of CNTs, scale bar 20 μm, **(b)** SEM image of the forest-like system in micro and nano scales, scale bar 500 nm, **(c)** TEM image of an individual multi-walled carbon nanotube (MWCNT), scale bar 20 nm.

In addition, these VACNT foams are characterized by an intrinsic gradient in functional properties, such as density and stiffness, which leads to sequential buckling when the samples are subjected to compressive loadings [37,42,123]. The typical curves obtained by testing the VACNT foams are shown in Figure 2.13.

2.4.8 Data reduction methodology and analysis

During impact, the force–time history (Figure 2.13 (a)) and the moiré fringe intensity modulation history (Figure 2.13 (b)) are recorded using the oscilloscope. The recorded data is smoothed for noise, using a low-pass filter, before analysis. A striker displacement of 25 μm (equivalent to the relative movement of a pitch of the gratings) corresponds to a full sinusoidal cycle in the intensity modulation recording (Figure 2.13 (b)). Hence, a peak-to-peak (or valley-to-valley) distance on the time axis (Figure 2.13 (b)) corresponds to the time taken for the movement of a pitch (25 μm). Similarly, peak-to-valley (or valley-to-peak) distance corresponds to a half pitch (12.5 μm). Differentiating the intensity data with respect to time and finding the peak and/or valley locations of that intensity-gradient profile allow us to find the time taken for a quarter-pitch movement (6.25 μm). As a result, a simple fringe counting produces the displacement history data (Figure 2.13 (c)) with a resolution of 6.25 μm.
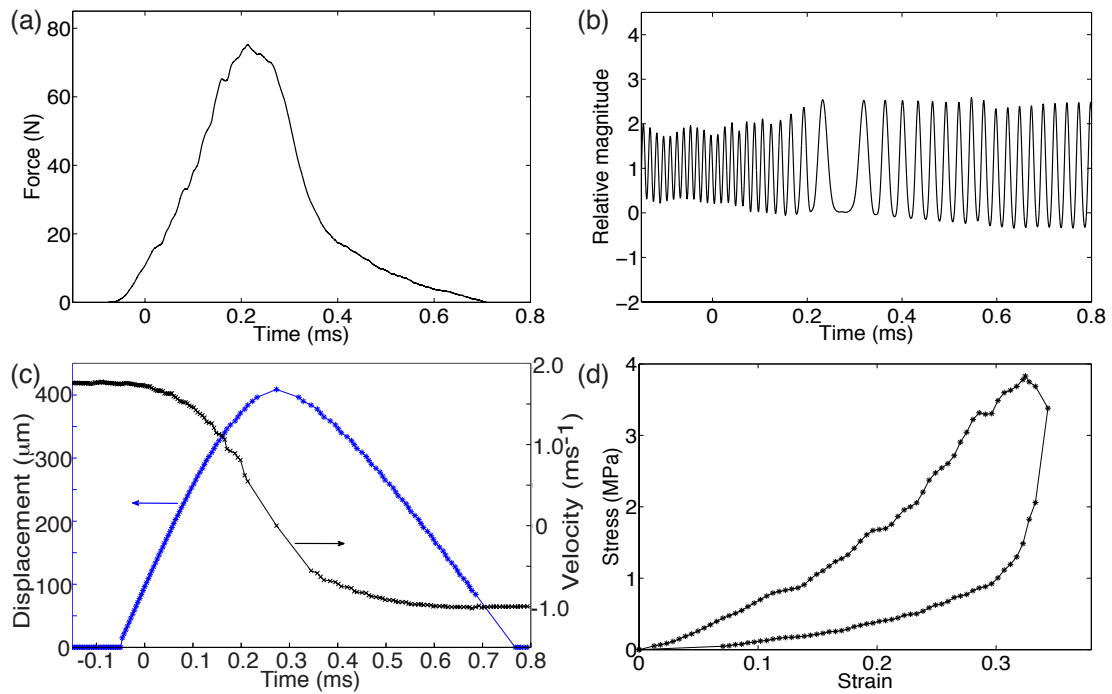
Figure 2.13. Experimental measurements of an impacted VACNT foam and data reduction: **(a)** force history, **(b)** intensity modulation of moiré fringes, **(c)** displacement and velocity histories, and **(d)** dynamic constitutive response.

Errors associated with data analysis are estimated to be much lower than a quarter pitch. An additional advantage of using geometric moiré as a displacement transducer is the availability of the velocity-time history (Figure 2.13 (c)). Impact, rebound velocities, displacement-rate, and nominal strain-rate during deformation are all readily available from the data. We use a central differentiation scheme to derive the velocity-time history from the displacement-time history.

To obtain the complete force-displacement profiles, the initial and final points of loading have to be found. We assume the noise level of the data recorded from the dynamic force sensor to be less than 100th of the force amplitude. We cut the tails of the force-time profile below this level at both ends and find the initial loading point from the initial gradient of the force-displacement data. After unloading, we measure the final (recovered) displacement from the high-speed image sequence. The input from the high-speed camera images is necessary in this case, since the tested samples rapidly unload

below one hundredth of the force amplitude, and continue to recover thereafter until detaching from the force-sensor.

Table 2.1. Physical (white background) and mechanical (gray background) properties of the VACNT foams tested.

Property/parameter	Specimen (A)	Specimen (B)
Diameter (mm)	5	5
Height (mm)	1.013	1.106
Bulk density (g cm^{-3})	0.258	0.232
Impact velocity (m s^{-1})	2.57	4.44
Rebound velocity (m s^{-1})	1.42	2.41
Nominal strain rate (s^{-1})	2537	4014
Coefficient of restitution	0.55	0.54
Peak stress (MPa)	7.59	17.28
Maximum strain	0.41	0.55
Energy dissipation (MJ m^{-3})	0.94	3.20
Loading modulus (MPa)	9.93	10.96
Unloading modulus (MPa)	204.93	331.14

The dynamic stress-strain diagram (Figure 2.13 (d)) can be obtained from the force-displacement profile, normalizing the force by the area of the specimen (nominal axial stress) and the displacement by the initial height of the specimen (nominal or engineering strain). Dynamic material properties such as the loading and unloading moduli, peak stress and maximum strain can be obtained from the dynamic constitutive response. From the maximum and recovery strains, the percentage recovery of foam-like energy absorbing materials can be calculated. Percentage recovery provides a measure for the resilience of the materials. The area included by the hysteresis of the stress-strain diagram provides the

energy dissipated by the material. From the ratio of rebound to impact velocities, the restitution coefficient which represents the elasticity of the impact can be obtained. These dynamic mechanical properties obtained for the two VACNT foams tested are summarized in Table 2.1. The dynamic stress-strain profiles corresponding to various loading-rates can be used to study the rate-sensitivity of the test material. Hence this experimental setup allows us to quantitatively study the impact response of energy absorbing materials as well as the fundamental micro-scale deformation characteristics of complex soft materials.

2.4.9   Comparison of displacement acquisition methods

In this section, we compare the dynamic constitutive response obtained from the two independent displacement measurements: (i) geometric moiré interferometry and (ii) high-speed microscopic imaging. Figure 2.14 shows the comparison of the dynamic constitutive response of two different VACNT foams impacted at 2.57 m s^{-1} (strain rate: 2537 s^{-1}), specimen (A) (Figure 2.14 (a)), and 4.44 m s^{-1} (strain rate: 4014 s^{-1}), specimen (B) (Figure 2.14 (b)). Here the nominal strain rates are calculated by dividing the impact velocity by the initial specimen height.

The displacement resolution of the geometric moiré interferometer is fixed by the grating pitch selected (and it is equal to 6.25 μm). Conversely, the displacement resolution obtained processing the high-speed image sequence depends primarily on three parameters: the spatial resolution of the images, the temporal resolution (frame-rate) and the rate of displacement (or the velocity) of the striker. The displacement resolution of our high-speed camera varied between 10-40 μm, for striker velocities of 1-6 m s^{-1}. In all cases tested, the moiré interferometry method reached a better displacement resolution and was able to capture stress fluctuations more accurately than the high-speed camera (Figure 2.14). The geometric moiré interferometry measured a larger maximum strain than the high-speed imaging technique, which can be attributed to tilting of the striker at the end of the loading phase. These deviations were calculated to be less than 5% of the total deformation.
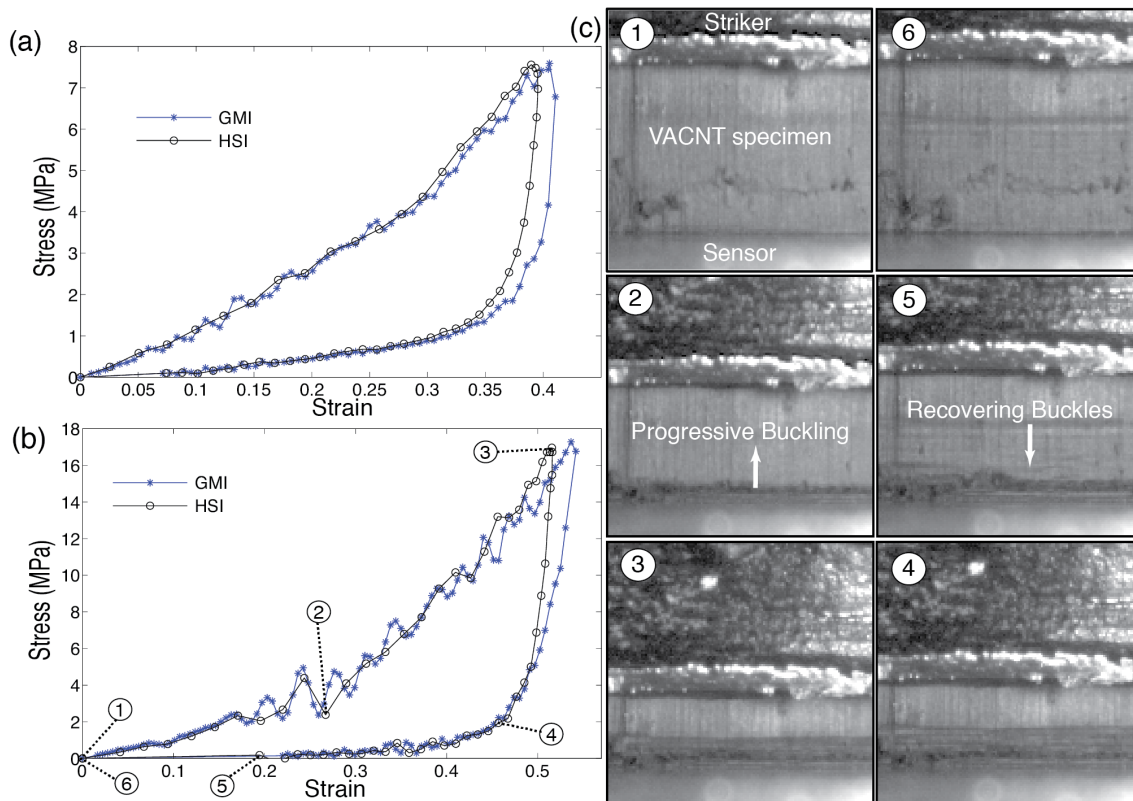
Figure 2.14. Comparison of dynamic constitutive response obtained with geometric moire interferometry (GMI) and high-speed imaging (HIS) at impact velocities **(a)** 2.57 m s^{-1} **(b)** 4.44 m s^{-1} **(c)** deformation micrographs of specimen (B) obtained with the high-speed camera.

The main advantage of using microscopic, high-speed image acquisition in the setup is the full field visualization of the samples' deformations. Complex materials often present strain localization, instabilities, and sequential deformation phenomena that would not be easily recognized or captured by direct global strain measurements. High-speed imaging enables the *in-situ* identification and characterization of the deformation mechanisms. For example, the series of frames extracted from the high-speed microscopic image sequence (Figure 2.14 (c)) demonstrate the ability to identify the formation of localized sequential buckling during loading and recovery of the VACNT sample. The high-speed image sequence on Figure 2.14 (c) corresponds to the VACNT foam (specimen (B)) impacted at 4.43 m s^{-1} and imaged at 128 x 256 pixel resolution and 150,000 fps frame-rate.

2.4.10 Material response

When the sample is first impacted by the striker, the compressive stress rises linearly with the strain. This deformation regime is followed by a nonlinear region primarily governed by the progressive buckling. The VACNT foams are characterized by an intrinsic density gradient along their height that is induced by the tCVD synthesis process. This graded functional property and the fibrous morphology of the foam leads to the formation of collective buckles of the VACNT bundles, which nucleate at the soft side of the specimen at the end of the initial linear stress-strain region. This localization of the deformation occurred independently of the sample's loading side, suggesting that the phenomenon derives from the intrinsic material property gradient.

As the specimen is compressed further, the stress rises with frequent instabilities until the striker reaches a zero velocity. The instabilities characterized by the negative slopes (or stress drops) in the stress-strain or stress-time curves correspond to the formation of buckles (see e.g., Figure 2.14 (c) images 2-3). This correlation can be seen in our experiments; however, limits arise when the size of the instabilities is below the spatial resolution of our imaging system and/or when the events progress too rapidly to be captured by the camera. A similar one-to-one correlation of instabilities in the force-history profiles with the formation of buckles has been reported for quasistatic compression tests [123]. It should be noted that due to these progressive instabilities, the peak stress reached during impact does not necessarily correspond to the maximum strain. In addition, the material exhibits a stiffening response, in which the compressive stress nonlinearly increases with the strain, as the specimen is compressed. This stiffening response arises from the increasing density gradient along the height of the specimen.

Once the maximum compressive strain is reached, as the striker reaches a zero velocity (Figure 2.14 (c) image 3), the VACNT foam starts releasing the stored energy and begins pushing the striker back. During this unloading phase, the unloading stress-strain path differs from the loading path, exhibiting a hysteresis. This deviation is evident particularly in the first 10% of the unloading strain, which corresponds to the progressive recovery of the buckles. When the specimen detaches from the force sensor along with

the striker, a full recovery of the specimen is observed (Figure 2.14 (c) image 6). This demonstrates the high resilience of the VACNT foams to impact.

The hysteresis included within the loading-unloading stress-strain loop accounts for the energy dissipated during the impact. The fundamental energy dissipation mechanisms and the reasons behind the presence of the hysteresis are still not well understood. Earlier studies suggested that the hysteresis derives from the presence of CNT-buckling [37], changes in the orientation or waviness of the individual nanotubes during the loading-unloading cycle [38], and friction between the individual and bundles of the tubes [37]. Using quasistatic compression cycles it was found previously that the energy dissipated by the VACNT foams deforming at an up to 80% strain is more than 200 times higher than the energy dissipated by commercial foams with similar densities [72]. The global dynamic behavior in the impact velocity range considered (1-6 m s^{-1}) is similar to the response observed in quasistatic compression cycles [37,42,123].